TRIBOLOGY

Designing metainterfaces with specified friction laws

Antoine Aymard, Emilie Delplanque, Davy Dalmas, Julien Scheibert*

Many devices, including touchscreens and robotic hands, involve frictional contacts. Optimizing these devices requires fine control of the interface's friction law. We lack systematic methods to create dry contact interfaces whose frictional behavior satisfies preset specifications. We propose a generic surface design strategy to prepare dry rough interfaces that have predefined relationships between normal and friction forces. Such metainterfaces circumvent the usual multiscale challenge of tribology by considering simplified surface topographies as assemblies of spherical asperities. Optimizing the individual asperities' heights enables specific friction laws to be targeted. Through various centimeter-scaled elastomer-glass metainterfaces, we illustrate three types of achievable friction laws, including linear laws with a specified friction coefficient and unusual nonlinear laws. This design strategy represents a scale- and material-independent, chemical-free pathway toward energy-saving and adaptable smart interfaces.

Despite centuries of investigation, a comprehensive understanding of friction is still lacking. For instance, predicting from first principles the value of the friction force, F, of a given dry contact interface remains out of reach, mainly because of the multiscale character of surfaces and the multiphysics nature of contact interactions (1). Thus, time- and resource-consuming experimental tests remain necessary to calibrate the frictional behavior of a contact interface as soon as any change is brought to the material pair, shape of the solids, loading conditions, surface finish, or environmental conditions. This inability to master friction is a major obstacle to the optimization of devices whose function relies on dry contact interfaces. For soft interfaces, these devices include sport accessories [e.g., racket coatings (2), shoe soles (3, 4)], robotic grasping devices (5–7), haptic feedback tools for virtual reality (8), and conveyor belts (9).

At the present time, surface functionalization is the main approach that is followed worldwide to provide contact interfaces with improved frictional capabilities (1, 10). It often consists of creating a certain surface topography at various length scales or adding a homogeneous or heterogeneous thin coating at the solid surface. Unfortunately, despite many successes in a variety of specific cases (11–15), this approach is still based on trial and error. It does not offer a general, systematic design strategy to convert a set of frictional specifications into an actual interface that offers the expected behavior. By circumventing the main pitfalls that make it difficult to understand friction in natural interfaces, we propose and validate a general design strategy to prepare multicontact interfaces with on-demand frictional features.

Université de Lyon, École Centrale de Lyon, CNRS, ENTPE, LTDS, UMR5513, 69130 Ecully, France.
*Corresponding author. Email: julien.scheibert@cnrs.fr

Results

General interface design strategy

To bypass the multiscale and multiphysics challenges of friction along rough interfaces, we propose a compromise between simplicity and richness in the surface description, by considering flat-flat contact interfaces between a smooth and a rough surface. Once the material pair is fixed, the designable feature of the interface is the topography of the rough surface, which is built as an ensemble of individual microasperities, with both well-controlled geometrical properties and calibrated contact and friction behaviors against the smooth counter surface. The richness of the emerging macroscale behavior stems from the countless possible combinations of geometrical properties of all individual asperities.

Just as the microstructures of the materials can be engineered to provide metamaterials with macroscale properties that are rarely found in nature [see (16–19) for mechanical metamaterials], we propose a design strategy (Fig. 1) to prepare contact interfaces with complex predefined frictional behavior. We denote these as metainterfaces. The strategy starts with a target friction law expressed as the macroscopic relationship $F_{target}(P)$ between the normal load P applied to the interface and the target macroscopic friction force F_{target}. This law is the input of an inversion step, the output of which is a geometrical description of the surface's topography, including the number of necessary asperities and the list of their individual properties (shape, size, height, position). The inversion is based on two main ingredients. First, the indentation and frictional behaviors of a single microcontact are obtained through a preliminary calibration (top-right illustration in Fig. 1), which may, but need not, be captured by an existing tribological model. Crucially, those calibrated behaviors contain any specific effect due to the manufacturing process, interface physicochemistry,

or surface contamination. Second, a suitable asperity-based friction model, able to predict the global frictional behavior as the collective response of the population of asperities, is identified. Depending on the expected relevant physics, the model can range from analytical (20–22) to numerical (23) through artificial intelligence [e.g., by extending the approaches of previous work (24, 25) to asperity-based descriptions of surface topography]. Based on the inverted asperities' geometries, a corresponding sample can be manufactured. The material and characteristic size of the prescribed asperities contribute to the selection of the relevant manufacturing method. Finally, shearing tests against the smooth counter surface enable determination of the resulting friction law, $F(P)$, and, through direct comparison with $F_{target}(P)$, assessment of the overall reliability of the workflow. Discrepancies with respect to the target friction law may arise from an incomplete calibration of the single asperity behavior, incorrect assumptions in the friction model, or manufacturing imperfections.

Applying the strategy to centimetric elastomer-glass interfaces

Although the generic flowchart shown in Fig. 1 is expected to be applicable to a large variety of frictional interfaces, the following scientific and technological choices represent only one example of how our design strategy can be implemented. First, we chose to work with contacts between polydimethylsiloxane (PDMS) and glass (26), a widely used pair of materials in contact mechanics and friction studies (1, 11). The behavior of sheared PDMS-glass, single sphere-plane contacts has been extensively characterized recently (27–30), which provides useful insights into the single-asperity laws that should be used in the friction model. In particular, the friction force, F, is found to be proportional to the contact area, A, through $F = \sigma A$, where σ is the frictional strength of the PDMS-glass interface. Predicting the macroscale friction force F is thus substantially simplified because, for a given σ, predicting F reduces to predicting the total contact area A of all microcontacts.

Second, as illustrated in Fig. 1, we chose to use a square lattice of 64 asperities as spherical caps, with a common radius of curvature $R = 526 \pm 5$ μm and distributed summit heights h_i. We obtained them by molding a PDMS slab onto an aluminum mold prepared with deterministic spherical holes using a sphere-ended cutting tool in a micromilling machine (26) (for a typical image of a PDMS textured sample, see Fig. 1). This method of preparing populations of spherical PDMS asperities has been successfully applied in the literature (31–33) but not used to design interfaces with predefined friction laws, as is done in this work. We have calibrated the indentation and shear behavior of single such microcontacts (26). Their normal

indentation is well captured by the classical Hertz model of a linear-elastic sphere–rigid plane contact (34) (Fig. 2B), with a composite elastic modulus E^* ($E^* = \frac{E}{1-\nu^2}$, where E and ν are the Young's modulus and Poisson's ratio of the PDMS, respectively). Consistent with previous work (27–30), the contact region is initially circular with an area a_0 but decreases anisotropically under shear, by ~10 to 15%, down to an area a_f (Fig. 2A) at the onset of sliding (static friction). The ratio $B = a_f/a_0$ thus represents the fraction of the initial contact area that remains when the contact is sheared and just about to slide. We found B to be independent of a_0 (Fig. 2C). We also confirmed the proportionality between the contact area and static friction force, $f = \sigma a_f$ (Fig. 2D).

The third choice we made was the type of friction model to be inverted. For the present proof of concept, we found that a very simple linear-elastic asperity-based model was sufficient. We considered N spherical linear-elastic asperities with common curvature radius, R, and composite elastic modulus, E^*, but distributed summit heights, h_i. This population of asperities is brought into contact with a rigid smooth plane, forming a number of microcontacts, which are each assumed to obey both Hertz's model (34) under pure compression and the calibrated friction behavior under shear. Microcontacts are assumed to be independent [see (26) for justification] such that their individual in-plane locations become irrelevant. The area of the ith microcontact is expressed as $a_{0,i} = \pi R(h_i - \delta)$ if $h_i \geq \delta$ and $a_{0,i} = 0$ if $h_i < \delta$, where δ is the separation between the rigid indenting plane and the base plane that supports the asperities. The macroscopic quantities are simple sums: $A_0 = \sum_{i=1}^{N} a_{0,i}$, $A_f = \sum_{i=1}^{N} a_{f,i}$, $P = \sum_{i=1}^{N} \frac{4E^*}{3\pi^{3/2}R} a_{0,i}^{3/2}$ (Hertz's model), and $F = \sum_{i=1}^{N} f_i = \sigma A_f$, where $A_f = BA_0$. The model parameter values were experimentally calibrated (26). Inverting the above friction model consists in determining a suitable list of heights h_i such that the predicted friction law satisfies specifications set a priori.

Interestingly, in the model, the friction law $F(P)$ can be rescaled as $\frac{F}{\sigma B}$ versus $\frac{P}{E^*}$, where the function relating $\frac{F}{\sigma B}$ and $\frac{P}{E^*}$ depends only on the geometrical parameters of the asperities, R and h_i, and not on the material parameters, σ, B, and E^*. Thus, in the following three examples, we illustrate the success of our design strategy using the material-independent relationship $\frac{F}{\sigma B}\left(\frac{P}{E^*}\right)$. This rescaled friction law characterizes solely the effect of surface topography, which is the actual interfacial quantity on which the design is performed.

Building a friction law from operating points

For our first example, we consider specifications in terms of a list of operating points $\left(\frac{P_i}{E^*}, \frac{F_i}{\sigma B}\right)$ through which the friction law $\frac{F}{\sigma B}\left(\frac{P}{E^*}\right)$ must pass. An infinity of suitable lists of asperity heights h_i exist as the solution to this
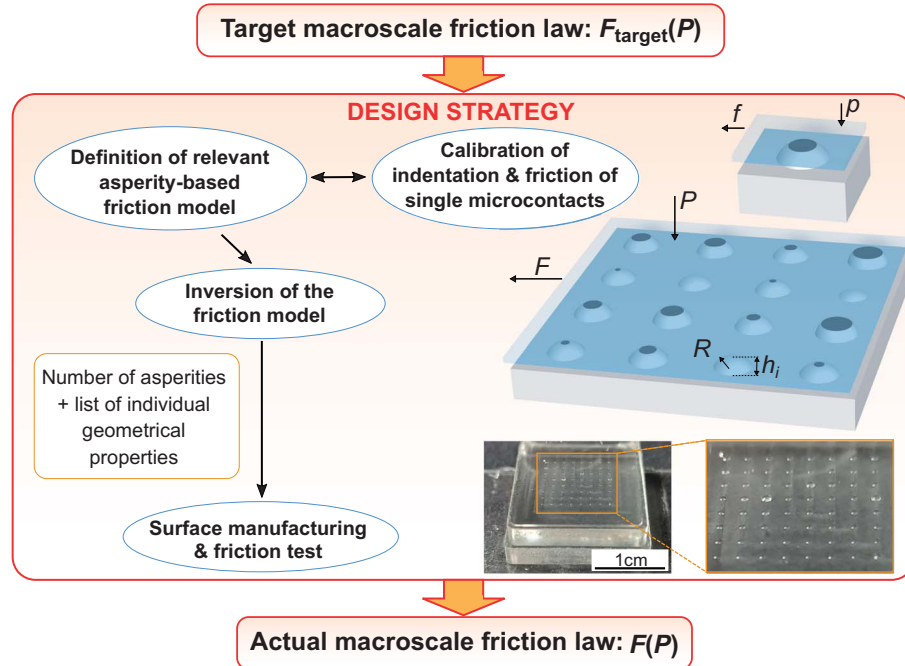

Fig. 1. Flowchart of the design strategy. Shown at the top right is an illustration of a single microcontact submitted to a normal force p and a friction force f. An illustration of a metainterface submitted to normal and friction forces, P and F, is shown at the middle right. Dark gray ellipses represent real contact regions. The topography is made of N asperities, each with specifically designed geometrical properties (here, spherical caps of height h_i and curvature radius R). At the bottom right is an image of a typical centimetric elastomer-based realization of such a textured sample. Photographs of metainterfaces can be found in Figs. 3 to 5.
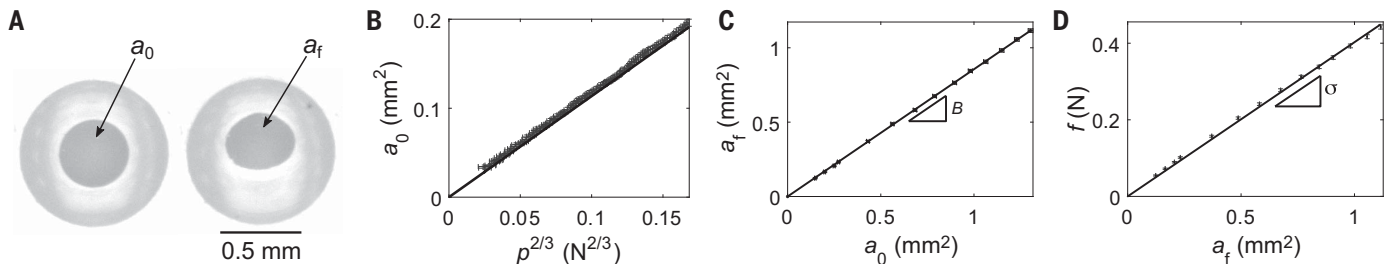

Fig. 2. Tribological calibration of single microcontacts. Illustrations for PDMS batch 1. (**A**) Images of a microcontact under normal load $p = 0.061$ N with no shear, initial area a_0 (dark central region) (left) and at the onset of sliding, area a_f (tangential force applied upward in the image plane) (right). (**B**) a_0 versus $p^{2/3}$, for three indentation experiments using three different samples (data points). The solid line is Hertz's prediction $a_0 = \pi\left(\frac{3Rp}{4E^*}\right)^{2/3}$ for $R = 526$ μm and $E^* = 1.36$ MPa [see (26) for information about how those values were determined]. (**C**) Typical evolution of a_f as a function of a_0 (data points). The solid line is the linear fit showing the existence of a constant area reduction ratio $B = a_f/a_0$. (**D**) Typical friction force f versus a_f (data points). The solid line is the linear fit showing the existence of a constant friction strength $\sigma = f/a_f$. Error bars are ±5 mN for p, ±(1 mN + 0.01f) for f, and ±2.8$\sqrt{\pi a} \times 10^{-6}$ m² for a_0 and a_f.
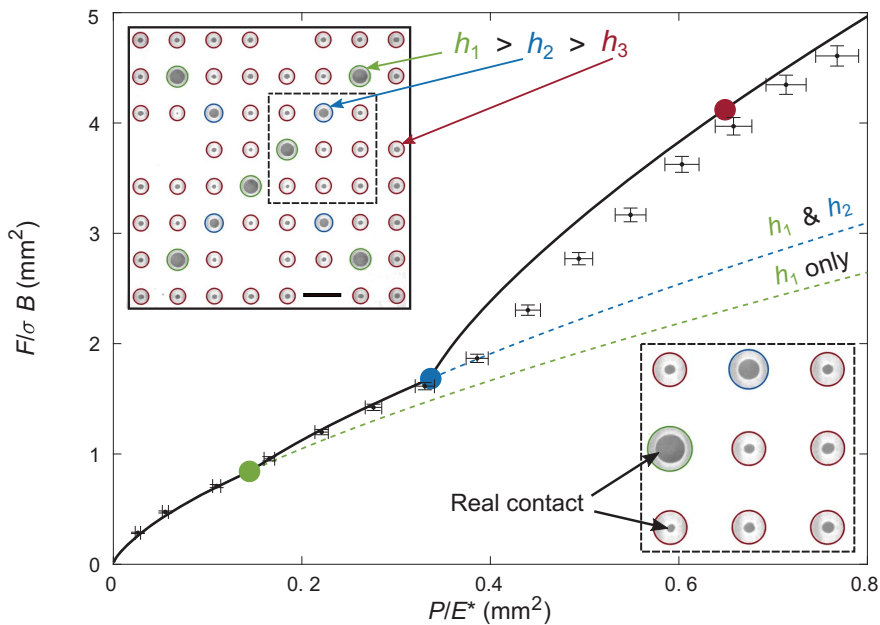
Fig. 3. Designing an interface that reaches three preset frictional operating points. The green, blue, and red disks represent targeted operating points. The black points represent measured friction law $\frac{F}{\sigma B}$ versus $\frac{P}{E^*}$. Error bars are calculated as described in (*26*). The solid line is the model prediction. Dashed lines are continuations of the two first branches of the solid line if the subsequent height levels of the asperities had not been populated. The top-left inset shows a full image of the unsheared contact under P = 0.92 N. Asperities at each of the three height levels ($h_1 > h_2 > h_3$) are circled with the same color as their associated operating point (main panel). Scale bar is 1.5 mm. The bottom-right inset shows a magnified view of the real contact of nine microcontacts (the region outlined by the dashed line in the top-left inset).
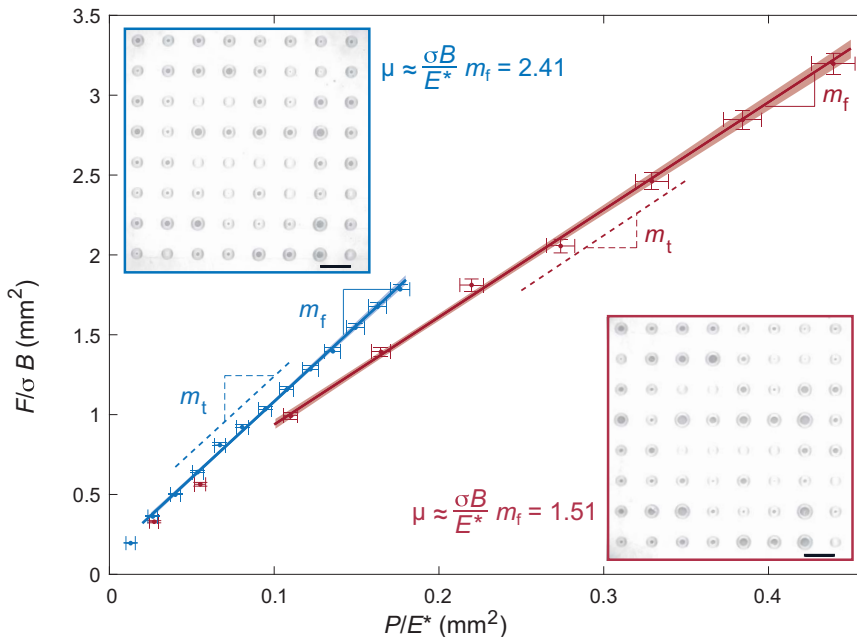

Fig. 4. Specifying the friction coefficient at a constant material pair. Experimental friction laws (data points) of two metainterfaces with exponential-like distributions of asperity heights (table S1). Error bars are as described in Fig. 3. Lines are linear fits of the data [over the last 12 (7) points for the blue (red) data]. The red and blue shaded regions around the lines represent the 68% confidence interval on the linear regression. The fitted slopes m_f of the rescaled laws, 6.73 ± 0.22 (red) and 9.53 ± 0.25 (blue) [which correspond to friction coefficients $\mu \approx \frac{\sigma B}{E^*} m_f = 1.51$ and 2.41 that are typical of PDMS-glass rough contacts (*27*, *29*)] match the targeted slopes (dashed lines), m_t = 6.87 (red) and 9.43 (blue), to better than 2.1%. The insets show typical photographs of the two metainterfaces under pure normal force P = 0.39 N (blue) or 0.93 N (red). Scale bars are 1.5 mm.

problem, each giving a different shape of the friction law between operating points. For pedagogical purposes, we adopted an inversion strategy (*26*) in which each operating point is reached using a single level of asperity height (fig. S1). To pass from the first (trivial) operating point (0, 0) to the next, one evaluates the maximum number of asperities with identical heights (first height level) required to approach the operating point from below and adds a single adjustment asperity whose height is selected to reach exactly the desired operating point. The procedure is repeated as many times as the number of additional operating points. As a result, upon normal loading, a prescribed number of new asperities enter the contact as soon as the previous operating point is reached. We applied this procedure to design a metainterface with a predicted three-branched friction behavior passing through three nonaligned operating points (Fig. 3). Our measurement points delineate a friction law that closely approaches the three target friction forces to better than 5% (2.5% for the first two points). This agreement shows that the design strategy can be successfully used to prepare real-life metainterfaces that target a nontrivial list of friction forces.

The latter design strategy can be extended to an arbitrary number of operating points (although sufficiently smaller than the number N of available asperities), opening the way to the design of interfaces with friction laws defined by many operating points. We expect that inversion procedures that are more versatile than the pedagogical one we present will be developed, for instance, those that invert not only h_i but also other geometrical quantities such as the curvature radius of each asperity.

Specifying the friction coefficient at a constant material pair

For our second example, we acknowledged that the most classical descriptor of the frictional properties of an interface is the value of its friction coefficient, μ. Commonly considered to be a characteristic of a pair of materials in contact, the friction coefficient does not relate to a particular operating point but rather to the global shape of the friction law. Indeed, unlike the curve shown in Fig. 3, in most natural or human-made interfaces, the friction law $F(P)$ is found to be linear [Amontons-Coulomb friction (*1*, *35*)], with μ being the slope of the law. Hence, we targeted linear friction laws with tunable slopes.

For surface topographies made of spherical asperities that obey Hertz's indentation law, as in our metainterfaces, a statistical framework relating the contact area A_0 to the normal load P exists [see Greenwood and Williamson's model (*20*)]. This framework predicts a linear $A_0(P)$ relationship when the asperities' heights, h_i, follow a probability distribution that is exponential ($e^{-h/\lambda}/\lambda$, where λ is the scale parameter

of the exponential). We adapted this model to account for the existence of a maximum asperity height h_m due to the finite number of asperities and extended it to predict linear-like friction laws [details in (26)]. In particular, we derived the value of the slope of $\frac{F}{\sigma B}\left(\frac{P}{E^*}\right)$ for large P: $m = \sqrt{\frac{\pi R}{\lambda}} \frac{1-e^{-x}}{\mathrm{erf}(\sqrt{x})-\frac{2}{\sqrt{\pi}}\sqrt{x}e^{-x}}$, where $x = h_m/\lambda$ and erf is the error function. m is a rescaled estimator for the friction coefficient of the interface ($m \approx \frac{E^*}{\sigma B}\mu$).

For illustrative purposes, we fixed R and h_m and targeted two different slopes m. Using the above expression of m, we identified the two λ that were suitable to generate two metainterfaces, each with one of the target slopes (26). The two friction laws that we obtained are linear, and their slopes match the predictions to better than 2.1% (Fig. 4). This agreement validates that our design strategy quantitatively enables the prescription of the slope of a linear friction law [after a nonlinear part at small P that is due to the finite value of h_m/λ and is responsible for a nonvanishing intercept; see (26)]. The slopes m that we achieved for the rescaled friction law $\frac{F}{\sigma B}\left(\frac{P}{E^*}\right)$ differ by a ratio of 1.42 (1.60 for the friction coefficients $\mu \approx \frac{\sigma B}{E^*}m$). For a discussion about the range of achievable friction coefficients, see (26). We emphasize that the results provide a practical way to tune the friction coefficient of a contact interface by manipulating the surface topography only, that is, without bringing any change to the bulk materials or physicochemistry of their surfaces.

Building friction laws with multiple specified linear branches

For our third example, we show that unnatural, nonlinear-shaped friction laws can also be designed, enabling one to go beyond Amontons-Coulomb–like friction. As an illustration, we targeted a succession of two linear branches with specified slopes, m_1 and m_2, and a crossover at a specified critical normal load, P_c/E^*. We first describe how such a friction law can be obtained [see (26)] using a weighted exponential distribution of heights, which generates two subpopulations of asperities. We then explain how to invert the law and find a suitable list of asperity heights, h_i [see (26)].

We demonstrate that such bilinear-shaped friction laws can indeed be achieved (Fig. 5) through two different realizations. As targeted, both realizations share the same two slopes, which are different by a ratio of 1.75, but have two different crossover normal loads, P_c/E^* (ratio 1.94). The slopes values are fulfilled by better than 5.2% (10% for the ratio of P_c/E^*), further demonstrating experimentally the success of our design strategy in satisfying quantitatively nontrivial friction prescriptions.

Discussion

Understanding friction in its generality remains a formidable challenge and has been

for centuries. Thus, controlling friction based on generic principles is often considered unreachable. Our work demonstrates that the friction of dry elastomer-based metainterfaces can actually be finely tuned when the surface topography is designed according to our proposed strategy (Fig. 1). We emphasize that our three examples far from exhaust the myriad possible variations around our design strategy, which provides a simple framework that enables friction-control opportunities, starting from, but not limited to, the universally used friction coefficient. Such topography-based control confirms, in particular, that the static friction coefficient is not a constant for a given pair of materials, as predicted by models (22, 23, 36) and observed in stick-slip experiments (37).

The potentially accessible friction laws $F(P)$ are countless, in terms of both their nonlinear shape and the way specifications are expressed (forces, slopes, etc.). Those alternative, richer prescriptions likely require the inversion of more topographic features than the individual asperities' heights, including their individual radii of curvature and in-plane locations. Such additional degrees of freedom should prompt the development and use of advanced friction models (22, 38) and inversion tools (25, 39) that are not limited to the analytical

approaches proposed here as pedagogical illustrations.

Static friction is not the only possible target functionality, because the design strategy can presumably be adapted to control other topography-related quantities, including interfacial stiffnesses and adhesion forces. Such extensions require different types of calibrations of individual microcontacts that are dedicated to those target properties. In this respect, note that in our experiments, the friction design strategy can be applied indifferently to the static friction force (as in Figs. 3 to 5) or sliding friction force [see (26)].

Our design strategy should be applicable to other material pairs than PDMS and glass. For materials whose contact remains elastic [see (26) for a criterion], the approach developed in our examples should hold, with material changes being accounted for by the rescaled, material-independent version of the friction law, $\frac{F}{\sigma B}\left(\frac{P}{E^*}\right)$. For nonelastic materials, qualitative changes might need to be brought to the calibrated microcontact behavior laws, friction model, and related inversions. For instance, for elastoplastic contacts, enriched asperity-based friction models are required (40, 41). In addition, the plasticity-induced irreversible modifications of the topography will likely affect all
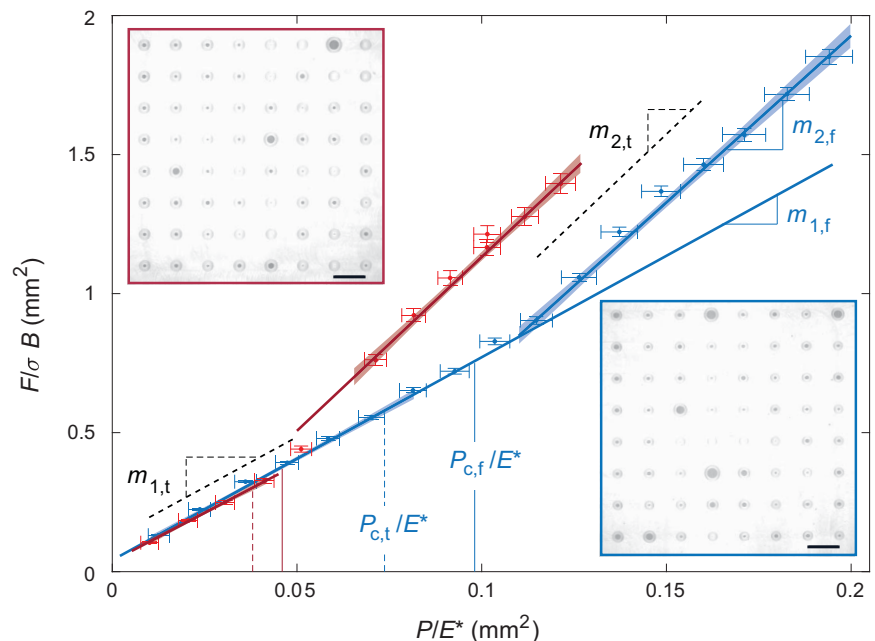

Fig. 5. Friction law made of two specified linear branches. Two experimental realizations of bilinear friction laws (data points) based on height distributions given by eq. S6 (table S2). Error bars are as described in Figs. 3 and 4. Solid lines are linear fits of each branch [six (four) first data points for the first branch of the blue (red) curve; eight (seven) last data points for the second branch of the blue (red) curve]. The red and blue shaded regions around the lines are as in Fig. 4. The fitted slopes m_f of both linear-like branches in each curve match the target slopes m_t (dashed black lines), 7.15 and 12.52, to better than 5.2%. Vertical lines show target ($P_{c,t}/E^*$, dashed lines) and observed ($P_{c,f}/E^*$, solid lines) crossover normal loads (in the same colors as the corresponding curves). Insets show typical photographs of the metainterfaces that underlie both friction laws under pure normal force $P = 0.23$ N (red) or 0.34 N (blue). The frame color refers to that of the corresponding friction law. Scale bars are 1.5 mm. See movie S1 for a qualitative illustration experiment on analogous metainterfaces.

successive uses of the metainterface such that the friction law is no longer a constant but rather a loading history–dependent function.

Irreversible changes of the topography may also arise as a result of wear-induced loss of material. Upon sliding, various wear mechanisms may occur, including progressive material removal that leads to blunted asperities and asperity-sized debris formation due to fracture processes (*42*). With such alterations of the surface topography, the behavior of metainterfaces will progressively deviate from the target one. In this context, evaluating the lifetime of metainterfaces as a function of the materials, roughness, and loading conditions will be an important step before use in any specific engineering application.

We expect our design strategy to be applicable over a large variety of length scales. We used asperities with a submillimetric radius of curvature that was obtained using micromilling. Larger asperities can be obtained in the same way or, for example, through 3D printing (*43*). For smaller scales, other well-established methods might be suitable, from laser ablation for asperities down to the micrometer scale (*44*) to micro- or nanolithography techniques at submicrometer scales (*45*). In all cases, experimental challenges include the reproducibility of the shapes of asperities (for microcontact calibration to be relevant), the level of accuracy of the manufactured asperity heights with respect to their prescribed values, and the potential misalignment between the two surfaces during the friction measurements [see (*26*) for a discussion of the latter two issues].

Many different types of frictional metainterfaces can be developed by using our design strategy, constituting a useful toolbox for designers of friction-based devices. By operating in optimized conditions, these devices should benefit from increased energy efficiency and lifetime. If further equipped with suitable sensors or actuators that bring relevant real-time changes to the topography, these metainterfaces could also become an asset in the development of smart systems (*46*) that incorporate functional solid contacts.

REFERENCES AND NOTES

1. A. I. Vakis *et al.*, *Tribol. Int.* **125**, 169–199 (2018).
2. M. Varenberg, A. Varenberg, *Tribol. Lett.* **47**, 51–56 (2012).
3. L. Damm *et al.*, *Footwear Sci.* **6**, 155–164 (2014).
4. J. Worobets, J. W. Wannop, *Sports Biomech.* **14**, 351–360 (2015).
5. M. R. Cutkosky, P. K. Wright, *Int. J. Robot. Res.* **5**, 20–37 (1986).
6. A. J. Spiers, B. Calli, A. M. Dollar, *IEEE Robot. Autom. Lett.* **3**, 4116–4123 (2018).
7. Y. Golan, A. Shapiro, E. Rimon, *IEEE Robot. Autom. Lett.* **5**, 2889–2896 (2020).
8. G. Millet, M. Otis, D. Horodniczy, J. R. Cooperstock, *Mechatronics* **46**, 115–125 (2017).
9. H.-W. Zhu *et al.*, *Powder Technol.* **367**, 421–426 (2020).
10. T. Ibatan, M. S. Uddin, M. A. K. Chowdhury, *Surf. Coat. Tech.* **272**, 102–120 (2015).
11. J. Scheibert, S. Leurent, A. Prevost, G. Debrégeas, *Science* **323**, 1503–1506 (2009).
12. B. Murarash, Y. Itovich, M. Varenberg, *Soft Matter* **7**, 5553–5557 (2011).
13. M. J. Baum, L. Heepe, E. Fadeeva, S. N. Gorb, *Beilstein J. Nanotechnol.* **5**, 1091–1103 (2014).
14. N. Li, E. Xu, Z. Liu, X. Wang, L. Liu, *Sci. Rep.* **6**, 39388 (2016).
15. J. Dufils *et al.*, *Surf. Coat. Tech.* **329**, 29–41 (2017).
16. M. Kadic, T. Bückmann, R. Schittny, M. Wegener, *Rep. Prog. Phys.* **76**, 126501 (2013).
17. B. Florijn, C. Coulais, M. van Hecke, *Phys. Rev. Lett.* **113**, 175503 (2014).
18. K. Bertoldi, V. Vitelli, J. Christensen, M. van Hecke, *Nat. Rev. Mater.* **2**, 17066 (2017).
19. J. U. Surjadi *et al.*, *Adv. Eng. Mater.* **21**, 1800864 (2019).
20. J. A. Greenwood, J. B. P. Williamson, *Proc. R. Soc. London Ser. A* **295**, 300–319 (1966).
21. O. M. Braun, M. Peyrard, *Phys. Rev. Lett.* **100**, 125501 (2008).
22. K. Thøgersen, J. K. Trømborg, H. A. Sveinsson, A. Malthe-Sørenssen, J. Scheibert, *Phys. Rev. E Stat. Nonlin. Soft Matter Phys.* **89**, 052401 (2014).
23. J. K. Trømborg *et al.*, *Proc. Natl. Acad. Sci. U.S.A.* **111**, 8764–8769 (2014).
24. G. Yang, Q. J. Li, Y. Zhan, Y. Fei, A. Zhang, *J. Comput. Civ. Eng.* **32**, 04018052 (2018).
25. P. Cinat, G. Gnecco, M. Paggi, *Front. Mech. Eng.* **6**, 29 (2020).
26. Materials and methods are available as supplementary materials.
27. R. Sahli *et al.*, *Proc. Natl. Acad. Sci. U.S.A.* **115**, 471–476 (2018).
28. J. C. Mergel, R. Sahli, J. Scheibert, R. A. Sauer, *J. Adhes.* **95**, 1101–1133 (2019).
29. R. Sahli *et al.*, *Phys. Rev. Lett.* **122**, 214301 (2019).
30. J. Lengiewicz *et al.*, *J. Mech. Phys. Solids* **143**, 104056 (2020).
31. V. Romero, E. Wandersman, G. Debrégeas, A. Prevost, *Phys. Rev. Lett.* **112**, 094301 (2014).
32. S. Yashima *et al.*, *Soft Matter* **11**, 871–881 (2015).
33. V. Acito, M. Ciavarella, A. M. Prevost, A. Chateauminois, *Tribol. Lett.* **67**, 54 (2019).
34. J. Barber, *Contact Mechanics*, Solid Mechanics and Its Applications Series, vol. 250 (Springer, 2018).
35. E. Popova, V. L. Popov, *Friction* **3**, 183–190 (2015).
36. J. Scheibert, D. K. Dysthe, *Europhys. Lett.* **92**, 54001 (2010).
37. O. Ben-David, J. Fineberg, *Phys. Rev. Lett.* **106**, 254301 (2011).
38. Y. Xu, J. Scheibert, N. Gadegaard, D. M. Mulvihill, *J. Mech. Phys. Solids* **164**, 104878 (2022).
39. T. Djourachkovitch, N. Blal, N. Hamila, A. Gravouil, *Comput. Struc.* **255**, 106574 (2021).
40. W. R. Chang, I. Etsion, D. B. Bogy, *J. Tribol.* **109**, 257–263 (1987).
41. H. Ghaednia *et al.*, *Appl. Mech. Rev.* **69**, 060804 (2017).
42. R. Aghababaei, D. H. Warner, J.-F. Molinari, *Nat. Commun.* **7**, 11816 (2016).
43. R. Sahli *et al.*, *Sci. Rep.* **10**, 15800 (2020).
44. B. Mao, A. Siddaiah, Y. Liao, P. L. Menezes, *J. Manuf. Process.* **53**, 153–173 (2020).
45. Z. Zhang, C. Geng, Z. Hao, T. Wei, Q. Yan, *Adv. Colloid Interface Sci.* **228**, 105–122 (2016).
46. M. A. McEvoy, N. Correll, *Science* **347**, 1261689 (2015).

SUPPLEMENTARY MATERIALS

science.org/doi/10.1126/science.adk4234
Materials and Methods
Figs. S1 to S3
Tables S1 and S2
References (*47–51*)
Movie S1

Submitted 21 August 2023; accepted 22 November 2023
10.1126/science.adk4234